Folding of Prestin's Anion-Binding Site and the Mechanism of Outer Hair Cell Electromotility

Xiaoxuan Lin[1], Patrick Haller[1,2], Navid Bavi[1,2], Nabil Faruk[1], Eduardo Perozo[1,2,3,4,*], Tobin R. Sosnick[1,4,5,*]

[1]Department of Biochemistry and Molecular Biology, [2]Center for Mechanical Excitability, [3]Institute for Neuroscience, [4]Institute for Biophysical Dynamics, [5]Prizker School for Molecular Engineering, The University of Chicago, Chicago, Illinois, USA

*Corresponding authors: trsosnic@uchicago.edu; eperozo@uchicago.edu.

Author Contributions: X.L., E.P., and T.R.S. designed research; X.L., P.H., N.B., and N.F. performed research; X.L., E.P., and T.R.S. analyzed data; and X.L., E.P., and T.R.S. wrote the paper.

Competing Interest Statement: The authors declare no competing interest.

Keywords: Mass spectrometry, hydrogen exchange, cochlear amplification, electromotility

Total number of manuscript pages, figures, supplementary pages, and tables:

	47
Manuscript pages, including main figures	17
Figures	5
Supplementary pages	24
Tables (in supplementary pages)	1

Description of supplementary material and file names:

1. Supporting Information Text 1: Heterogeneity and HDX kinetics.
2. Supporting Information Text 2: Combining HDX-MS and cryo-EM in structural biology.
3. Figure S1: Volcano plot analysis of HDX for prestin and SLC26A9 in response to Cl^- binding.
4. Figure S2: Site-resolved protection factors for prestin and SLC26A9 obtained using PyHDX.
5. Figure S3: PyHDX fitting supports that prestin exhibits helix fraying at the N-terminus of TM3 and mild cooperativity at the intracellular portion of TM6.
6. Figure S4: Mammalian prestin has a conserved and helix-destabilizing proline 136 on TM3.
7. Figure S5: HDX-MS sequence coverage and measurements for prestin and SLC26A9 in Cl^-.
8. Figure S6: Regions unresolved in cryo-EM structures are unfolded in all conditions examined.
9. Figure S7: HDX for prestin occurs via EX2 mechanism.
10. Figure S8: Heterogeneity and HDX kinetics in TM1 and TM9.
11. Figure S9: Deuterium uptake curves for all peptides covering prestin's transmembrane domain.
12. Figure S10: Deuterium uptake curves for all peptides covering SLC26A9's transmembrane domain.
13. Table S1: Biochemical and statistical details for HDX

Abstract

Prestin responds to transmembrane voltage fluctuations by changing its cross-sectional area, a process underlying the electromotility of outer hair cells and cochlear amplification. Prestin belongs to the SLC26 family of anion transporters yet is the only member capable of displaying electromotility. Prestin's voltage-dependent conformational changes are driven by the putative displacement of residue R399 and a set of sparse charged residues within the transmembrane domain, following the binding of a Cl^- anion at a conserved binding site formed by amino termini of the TM3 and TM10 helices. However, a major conundrum arises as to how an anion that binds in proximity to a positive charge (R399), can promote the voltage sensitivity of prestin. Using hydrogen-deuterium exchange mass spectrometry, we find that prestin displays an unstable anion-binding site, where folding of the amino termini of TM3 and TM10 is coupled to Cl^- binding. This event shortens the TM3-TM10 electrostatic gap, thereby connecting the two helices such that TM3-anion-TM10 is pushed upwards by forces from the electric field, resulting in reduced cross-sectional area. These folding events upon anion-binding are absent in SLC26A9, a non-electromotile transporter closely related to prestin. We also observe helix fraying at prestin's anion-binding site but cooperative unfolding of multiple lipid-facing helices, features that may promote prestin's fast electromechanical rearrangements. These results highlight a novel role of the folding equilibrium of the anion-binding site, and helps define prestin's unique voltage-sensing mechanism and electromotility.

Introduction

Hearing sensitivity in mammals is sharply tuned by a cochlear amplifier associated with electromotile length changes in outer hair cells[1]. These changes are driven by prestin (SLC26A5), a member of the SLC26 anion transporter family, which converts voltage-dependent conformational transitions into cross-sectional area changes, affecting its footprint in the lipid bilayer[2]. This process plays a major role in mammalian cochlear amplification and frequency selectivity, with prestin knockout producing a 40-60 dB signal loss in live cochleae[3]. Unlike most molecular motors, where force is exerted from chemical energy transduction, prestin behaves as a putative piezoelectric device, where mechanical and electrical transduction are coupled[4]. As a result, prestin functions as a direct voltage-to-force transducer. Prestin's piezoelectric properties are unique among members of the SLC26 family, where most of the SLC26 homologs function as anion transporters.

Recent structures determined by cryo-electron microscopy (cryo-EM) have sampled prestin's conformational space under various anionic environments and located the anion-binding site at the electrostatic gap between the amino termini of TM3 and TM10 helices[5–7]. This anion-binding pocket is highly conserved, and is influenced by surrounding hydrophobic residues in TM1 and by a fixed positive charge from residue R399 on TM10. Movements of this binding site are coupled to the complex reorientation of the core domain relative to the gate domain[5,6], reminiscent of the conformational transitions in transporters displaying an elevator-like mechanism[8]. Prestin exhibits minimal transporter ability yet is structurally similar to the non-electromotive anion transporter SLC26A9 (sequence identity = 34%; Cα RMSD = 3.4 Å for the transmembrane domain (TMD), PDB: 7S8X and 6RTC)[7,9,10]. Questions remain as to the molecular

basis underlying the distinct functions of the two proteins. Importantly, the role of bound anions, which is required for prestin electromotility[11], is still elusive.

Prestin's voltage dependence is tightly regulated by intracellular anions of varying valence and structure[12,13], whereas anion affinity is also regulated by voltage and tension[14]. These phenomena suggest that anions, rather than behaving as explicit gating charges, may serve as allosteric modulators[14]. Incorporating a fixed charge alternative to a bound anion through an S398E mutation preserves prestin's nonlinear capacitance (NLC) but results in insensitivity to salicylate, a strong competing anionic binder[7]. Except for residue R399 near the anion-binding site, charged residues located in the TMD distribute towards the membrane-water interface[5–7] and display minimal contributions to the total gating charge estimated from NLCs[15]. Electrostatic calculations show that R399 has a strong contribution to the local electrostatics at the anion-binding site, by providing ~40% of the positive charge at the bilayer mid-plane[5]. However, the existing structural and functional data cannot explain why prestin's voltage dependence requires close proximity of both a negative charge (the bound anion or S398E)[11] and a positive charge (R399[5,16]). The resolution of this conundrum will define an essential step towards our understanding of prestin's unique voltage-sensing mechanism.

Here we studied the influence of anion-binding on the dynamics and structural changes of prestin as a function of anions (Cl^-, SO_4^{2-}, salicylate, and Hepes) via hydrogen-deuterium exchange mass spectrometry (HDX-MS). The Hepes condition was achieved by Cl^- removal (dialysis), which inhibits prestin's NLC[11], and hence induced an apo state. We assumed a low affinity of Hepes anions due to their large size. Furthermore, prestin's NLC shifts to depolarized potentials in a Hepes-based buffer, suggesting that at 0 mV, prestin adopts a more expanded state that is coupled to low anion affinity[12,13]. By comparing the dynamics of prestin with its close non-piezoelectric relative, the anion transporter SLC26A9, we identified distinct features unique to prestin, including a relatively unstable anion-binding site that folds upon binding, thereby allosterically modulating the dynamics of the TMD. In contrast, the stability and hydrogen-bond pattern of SLC26A9's anion-binding site were minimally affected by anion binding, albeit displaying high similarities to prestin in both structure and sequence. We observed fraying of the helices involved in the binding site whereas cooperative unfolding of multiple lipid-facing helices, which may explain prestin's fast and large-scale motions. These results highlight the significance of the anion-binding site's folding equilibrium in defining the unique properties of prestin's voltage dependence and electromotility.

Results

We carried out HDX measurements on dolphin prestin and mouse SLC26A9 solubilized in glyco-diosgenin (GDN) at either pD_{read} 7.1, 25 °C or pD_{read} 6.1, 0 °C (**Table S1**). These conditions provided an effective labeling time window spanning seven log units, allowing us to determine HDX rates and protection factors (PFs) throughout the protein[17]. Under our experimental conditions, the observed HDX rates report on the stability, as exchange occurs mostly via EX2 kinetics (**Supporting Information Text 1**). The HDX data are presented in terms of the relevant region with the specific sequence and peptide noted in parentheses (**Materials and Methods**), e.g., the N-terminus of prestin's TM10 ($Region_{394–397}$: $Peptide_{392–397}$). Although we mostly focused on the

anion-binding site, we also obtained comparative thermodynamic information throughout the two proteins (**Supporting Information Text 2**).

<u>Prestin's anion-binding site is less stable than SLC26A9's.</u>

To examine the effect of anion binding to the dynamics of prestin and SLC26A9, we dialyzed the proteins purified in Cl^- into a Hepes buffer lacking other anions. Cl^- removal resulted in distinct stability changes for prestin and SLC26A9, manifested by significant HDX acceleration for prestin

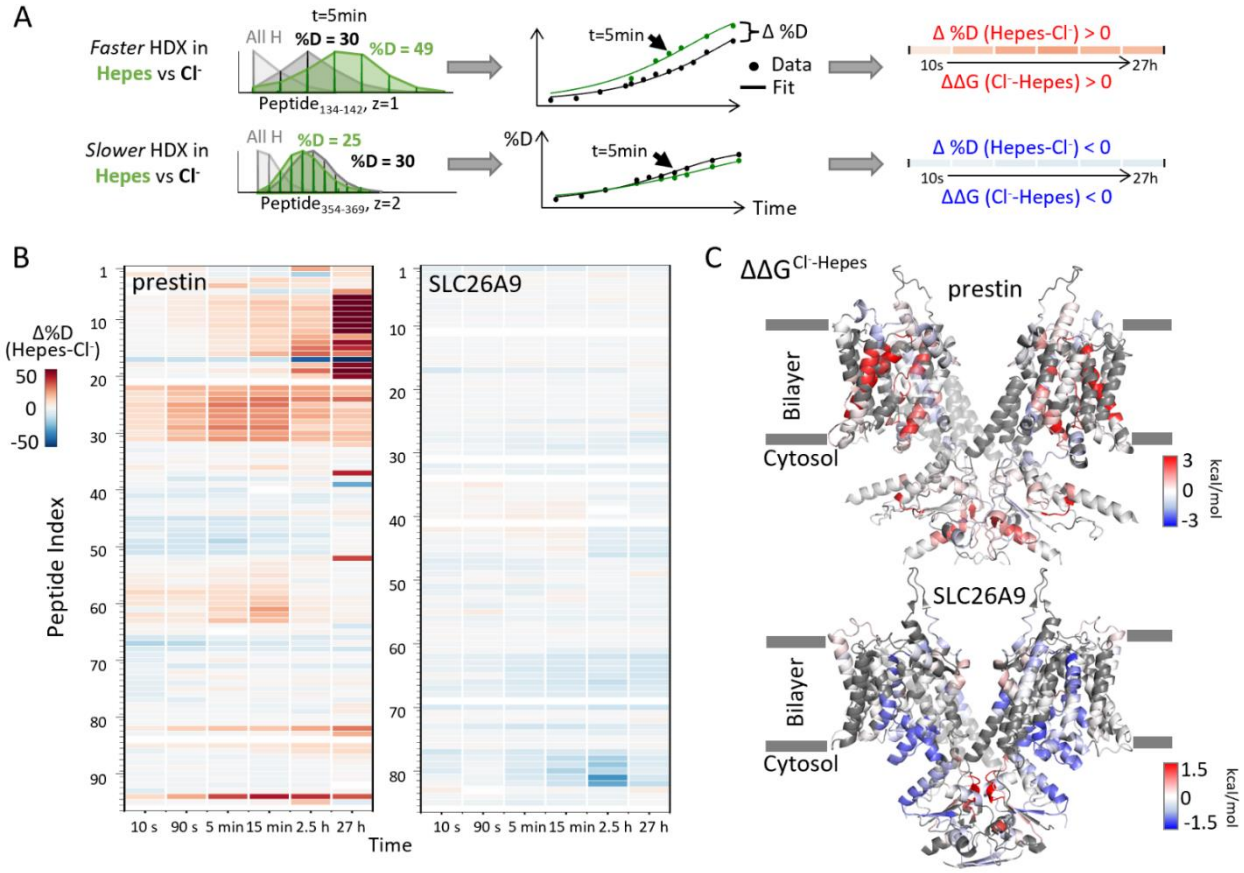

Figure 1: Distinct HDX response of prestin and SLC26A9 to Cl^- binding. (A) HDX data analysis to obtain **(B)** and **(C)**. One example peptide is shown in cases where HDX becomes faster or slower in Hepes (the apo state) compared to in Cl^-. Deuteration levels are obtained from the mass spectra. Here spectra for the undeuterated peptide (grey) and after 5 min HDX labeling in Cl^- (black) and Hepes (green) are shown as an example. The resulting deuterium uptake plots are used to generate the differential deuteration heatmaps in **(B)**. Changes in free energy of unfolding (ΔΔG) in **(C)** are calculated after fitting the data with a stretched exponential (**Materials and Methods**)[17]. **(B)** Heatmaps showing the difference in deuteration levels at each labeling time for all TMD peptides of prestin and SLC26A9 measured in Hepes compared to Cl^-. Peptide sequences corresponding to peptide indexes can be found in Fig. S9 & Fig. S10. **(C)** The ΔΔGs in Hepes compared to Cl^- for full-length prestin and SLC26A9 mapped onto the structure (PDB 7S8X and 6RTC). Red and blue indicate increased and decreased stability upon Cl^- binding, respectively. Following regions of the left subunits are shown as low transparency to highlight the binding site – prestin: TM5 and TM12-14; SLC26A9: TM5 and TM13-14. Regions with no fitting results are in grey.

while mild HDX slowing for SLC26A9 (**Fig. 1 & Fig. S1**). These HDX effects indicate that anion binding induced global stabilization for prestin while slight destabilization for SLC26A9 (**Fig. 1**).

Among the observed HDX responses for prestin, the HDX acceleration at the anion-binding pocket appeared to be the most pronounced and indicates local stabilization induced by anion binding (**Fig. 2A**). In detail, HDX accelerated by 20-fold for the N-termini of both TM3 ($\text{Region}_{136\text{-}142}$: $\text{Peptide}_{134\text{-}142}$ + 9 other peptides) and TM10 ($\text{Region}_{394\text{–}397}$: $\text{Peptide}_{392\text{–}397}$) (**Fig. 2A & Fig. S9.22-9.31**). This HDX change translates to a difference in free energy of unfolding (ΔΔG) by at least 1.8 kcal/mol; $\Delta\Delta G_{\text{Cl-apo}}^{\text{binding site}}$ = 1.8 kcal/mol. At least four residues in the middle of TM1 exhibited faster HDX ($\text{Region}_{90\text{-}101}$: $\text{Peptide}_{88\text{-}101}$ + 10 other peptides), collectively by 350-fold;

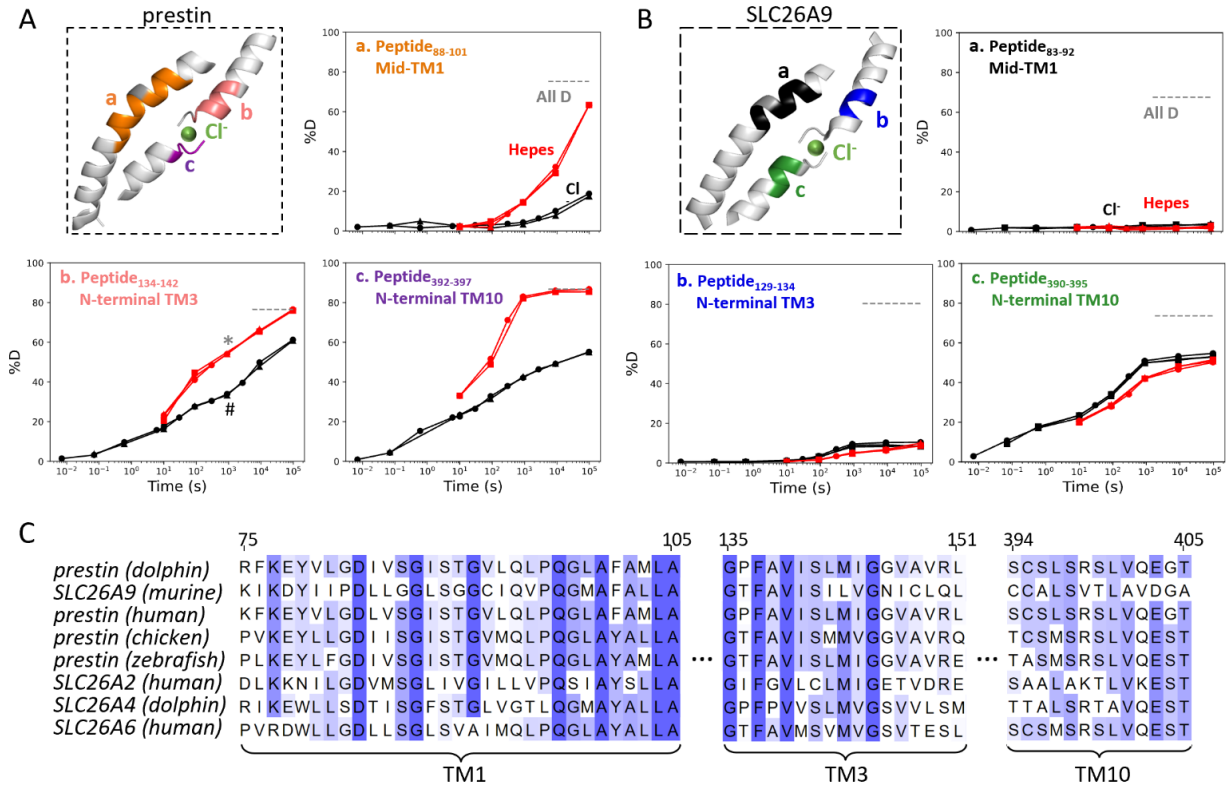

Figure 2: The anion-binding pockets for prestin and SLC26A9 exhibit distinct stability changes upon Cl^- binding, albeit highly conserved. (A-B) Cl^- binding stabilizes prestin's anion-binding pocket **(A)** but mildly affects SLC26A9's **(B)**. The structure shows the anion-binding pocket (TM1, TM3, and TM10) with the putative position of the bound Cl^-. Colored regions correspond to peptides whose deuterium uptake plots are shown (prolines are colored in grey) when the protein is in Cl^- (black) and in Hepes (red). Grey dashed lines indicate deuteration levels in the full-D control. Data from two and three biological replicates are shown for prestin in Cl^- and Hepes, respectively. Data from three technical replicates are shown for SLC26A9. Replicates are shown as circles, triangles, and squares. Some replicates are superimposable and hence not observable. The symbols (* and #) in **(A.b)** denote data points used in **Fig. 3B**. **(C)** Sequence alignment using Clustal Omega of prestin and close SLC26 transporters across species for the anion-binding pocket. Shades of blue indicate degree of conservation.

101 $\Delta\Delta G^{TM1}_{Cl\text{-}apo}$ = 3.5 kcal/mol (**Fig. 1A & Fig. S9.6-9.16**). The TM1 region with accelerated HDX included
102 L93, Q97, and F101, residues that are known to participate in the binding pocket[5,6,18].
103 SLC26A9 exhibited similar stability as prestin in Cl^- for the majority of the TMD, except for
104 the N-terminal TM3 ($Region_{131\text{-}134}$: $Peptide_{129\text{-}134}$) which exchanged at least 100-fold slower than
105 that of prestin's ($Region_{136\text{-}142}$: $Peptide_{134\text{-}142}$) (**Fig. 2**). This difference in HDX points to a relatively
106 unstable anion-binding site of prestin as compared to SLC26A9; $\Delta\Delta G^{N\text{-terminal TM3}}_{SLC26A9\text{-}prestin}$ > 2.8 kcal/mol,
107 and was also seen in the site-resolved PFs that were obtained by deconvoluting the HDX-MS data
108 using PyHDX[19] (**Fig. S2**).

109 Compared to the 20~350-fold HDX acceleration observed at prestin's binding site upon
110 Cl^- removal, HDX of SLC26A9's binding pocket was only affected mildly (**Fig. 2B**). These included
111 a slight slowing in HDX for the N-termini of TM3 ($Region_{131\text{-}134}$: $Peptide_{129\text{-}134}$) and TM10
112 ($Region_{392\text{-}395}$: $Peptide_{390\text{-}395}$) (**Fig. 2B**). The TM1 ($Region_{72\text{-}92}$: $Peptide_{83\text{-}92}$ + 10 other peptides)
113 continued to remain undeuterated even after 27 h (**Fig. 2B & Fig. S10.4-10.14**), emphasizing the
114 intrinsic high stability of SLC26A9's anion-binding pocket.
115 Although the anion-binding pocket is highly conserved and structurally similar across
116 members of the SLC26 family and SLC26A5 families (**Fig. 2C**), mammalian prestin is the only
117 member capable of displaying eletromotility[20]. Hence, the distinct stability responses we observe
118 for dolphin prestin and mouse SLC26A9 point to a prestin's unique adaptation as a motor protein.
119 In addition to the binding pocket, we observed stability changes in various regions of the
120 TMDs for prestin and SLC26A9 that may explain their distinct functions. For prestin, anion binding
121 resulted in stabilization for the intracellular cavity but destabilization for regions facing the
122 extracellular milieau (**Fig. 1C & Fig. S1A**). The stabilizing effects for the cytosol-facing regions
123 were manifested by HDX acceleration upon Cl^- removal at the linker between TM2 and TM3, and
124 the intracellular portions of TM7, TM8, & TM9 ($Region_{128\text{-}135}$, $Region_{284\text{-}294}$, & $Region_{354\text{-}375}$) (**Fig.**
125 **S9.22-9.27, S9.58-9.64, S9.82-9.87**). In contrast, HDX slowed for the regions facing the
126 extracellular environment, namely the extracellular ends of TM5b, TM6, and TM7 ($Region_{250\text{-}262}$
127 & $Region_{309\text{-}316}$) (**Fig. S9.45-9.51, S9.66-9.68, S9.71**). However, for SLC26A9, anion binding
128 destabilized the cytosol-facing regions, as HDX slowed by ~5-fold upon Cl^- removal for the
129 intracellular ends of TM8, TM9, and TM12 ($Region_{351\text{-}369}$ & $Region_{440\text{-}455}$) (**Fig. 1C, Fig. S1B, & Fig.**
130 **S10.62-10.63, S10.77-10.82**). The distinct thermodynamic consequences of anion binding for
131 prestin and SLC26A9 point to a distinct molecular basis underlying their different functions as a
132 motor and a transporter, respectively.

133

134 <u>Anion binding drives the folding of prestin's binding site.</u>
135 In the apo state of prestin, the 20-fold HDX acceleration for the binding site (**Fig. 2A**) is consistent
136 with a process of local destabilization, even unfolding, or increased solvent accessibility as the
137 region becomes exposed to the intracellular water cavity[5]. To investigate these possibilities, we
138 measured prestin's HDX in response to a chaotrope, urea, which destabilizes proteins by
139 interacting with backbone amides[21]. In a background of 360 mM Cl^-, the addition of 4 M urea

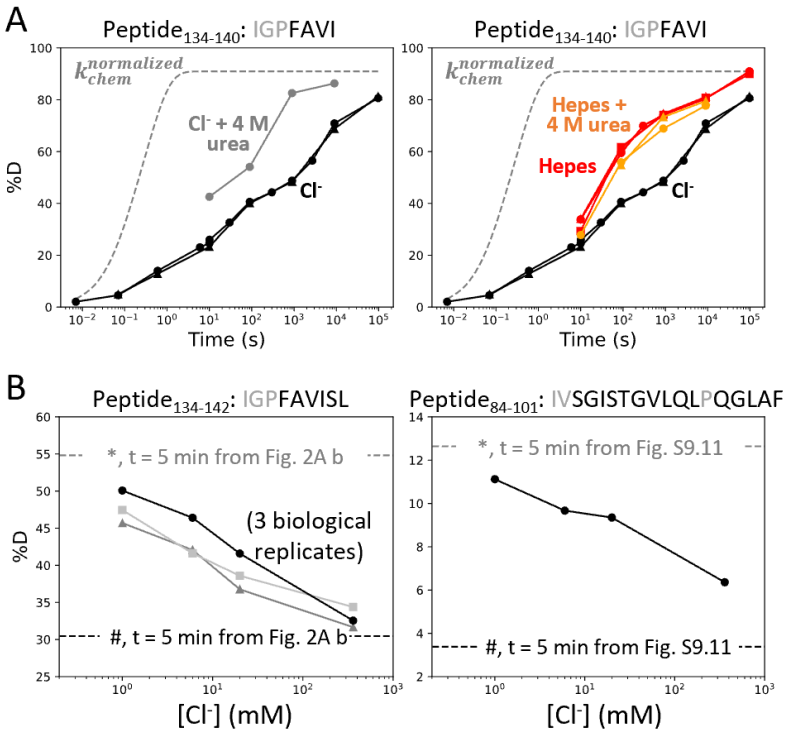

Figure 3: Anion binding folds and stabilizes prestin's binding site. (A) Deuterium uptake plots for the N-terminus of TM3 ($Peptide_{134-140}$) measured in the absence and presence of 4 M urea, in a background of (**Left**) Cl^- and (**Right**) Hepes. Replicates (circles, triangles, and squares): 2 in Cl^-, 3 in Hepes, 2 in Hepes with urea, biological. Grey dashed curves represent deuterium uptake with k_{chem}[34,35], normalized with the back-exchange level. **(B)** Deuteration levels for (**Left**) the N-terminus of TM3 ($Peptide_{134-142}$) in three biological replicates and for (**Right**) TM1 ($Peptide_{84-101}$) after 5 min labeling upon titrating Cl^- to apo state of prestin. Dashed lines indicate deuteration levels at t = 5 min (* and # for apo and Cl^--bound states, respectively) taken from **Fig. 2A.b** and **Fig. S9.11**. Residues in grey denoted in the peptide sequence do not contribute to the deuterium uptake curve.

accelerated HDX for the N-terminus of TM3 ($Region_{137-140}$: $Peptide_{134-140}$) by 20-fold (**Fig. 3A**), suggesting that this region was destabilized and accessible to urea in its exchange-competent state. In apo prestin, however, the PF at the N-terminus of TM3 was unaffected by urea (after accounting for the known ~50% slowing of the intrinsic exchange rate[21], k_{chem}) (**Fig. 3A**), arguing that this region was already unfolded prior to the addition of urea[22].

We note that in apparent contradiction to our inference that the N-terminus of TM3 was unfolded in the apo state, its HDX was ~100-fold slower than k_{chem}. Such apparent PF for an unfolded region has been reported when it is located inside an outer membrane β-barrel, rationalized by the region having a lower effective local concentration of the HDX catalyst, $[OD^-]$, than in bulk solvent[23,24]. For prestin, we propose that detergent molecules in the micelle can restrict the access of OD^- to amide protons and thus produce the apparent PF for the unfolded N-terminus of TM3.

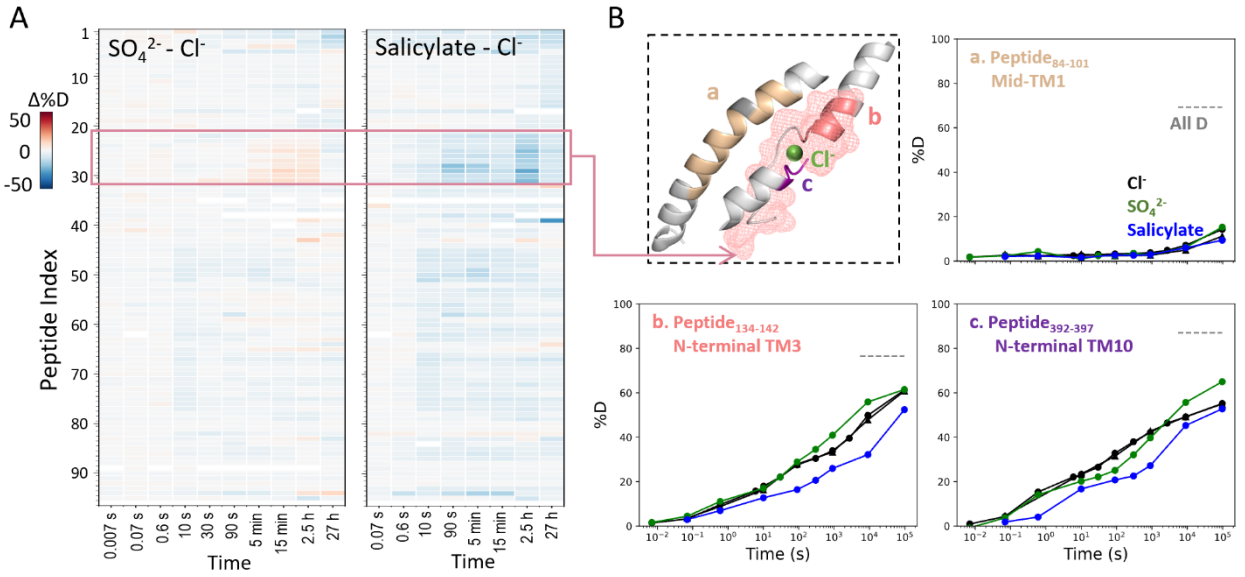

Figure 4: Prestin's dynamics are regulated by anions of varying identities. (A) Heatmaps showing the difference in deuteration levels at each labeling time for all TMD peptides measured in SO_4^{2-} or salicylate compared to Cl^-. Peptide sequences corresponding to peptide indexes can be found in Fig. S9. **(B)** The structure shows the anion-binding pocket with the putative position of the bound Cl^-. The pink mesh highlights the region with the greatest HDX response to binding to various anions. Colored regions correspond to peptides whose deuterium uptake plots are shown (prolines are colored in grey) when the protein is in Cl^- (black, two biological replicates shown in circles and triangles), SO_4^{2-} (green), and salicylate (blue). Grey dashed lines indicate deuteration levels in the full-D control.

The folding reversibility of the anion-binding site was evaluated by tracking the HDX for 5 min after titrating in Cl^- to apo prestin. Deuteration levels for the N-terminus of TM3 (Region$_{137-140}$) decreased with increasing Cl^- concentration (**Fig. 3B**), suggesting reversible folding upon Cl^- binding. Similar behavior was seen in the middle of TM1 (Region$_{86-101}$: Peptide$_{84-101}$) as Cl^- binding stabilized the binding pocket (**Fig. 3B**).

We also examined prestin's stability in its intermediate states, obtained by replacing Cl^- anions with SO_4^{2-} and salicylate[5,6]. When SO_4^{2-} is the major anion, prestin's HDX was nearly identical as in Cl^-, except for a slightly faster HDX at the anion-binding site (Region$_{128-142}$ and Region$_{394–397}$) at labeling times longer than 10^3 s (**Fig. 4**). This mild HDX response suggested a slightly destabilized binding site while the remaining regions retained normal dynamics as in Cl^-. In the presence of salicylate, HDX slowed across the TMD, with the greatest effect seen at the anion-binding site (10-fold; $\Delta\Delta G^{\text{binding site}}_{\text{salicylate-Cl-}} = 1.4$ kcal/mol) (**Fig. 4**), indicating that salicylate binding to prestin globally stabilized the TMD, primarily at the anion-binding site. These stability changes provide a thermodynamic context to the cryo-EM structures[5].

<u>Incremental unfolding of prestin's binding site versus cooperative unfolding of the lipid-facing helices</u>.

Our broad HDX time range and dense sampling allowed us to observe effects at the residue level. In particular, the binding site of prestin (Region$_{128\text{-}140}$ and Region$_{394–397}$) exhibited a broad deuterium uptake curve in Cl^-, indicative of helix fraying where exchange of deuterium occurs from multiple states that differ by one hydrogen bond (**Fig. 5A**). Such HDX pattern is consistent with the associated residues undergoing sequential unfolding with distinct PFs (i.e., stability). Site-resolved PFs obtained using PyHDX[19] support that the stability increased residue-by-residue for TM3 for amide protons located further away from the substrate (**Fig. S3A**). This gradual increase in residue stability along the helices is indicative of helix fraying starting from prestin's binding site.

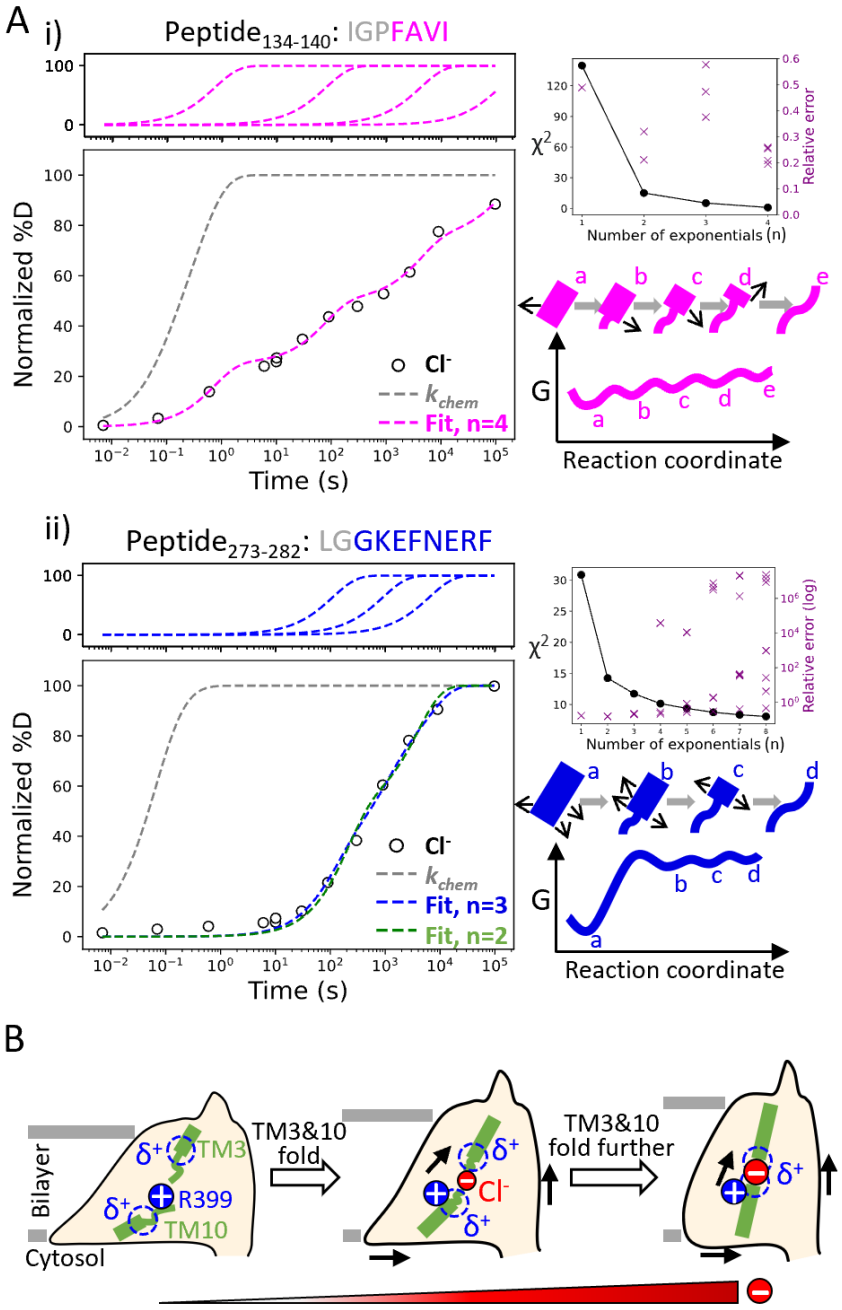

Figure 5: Helix folding cooperativity and the proposed mechanism for prestin's electromotility. (A) Left: Deuterium buildup curves for **(i)** the N-terminal TM3 ($Peptide_{134-140}$) and **(ii)** the intracellular portion of TM6 ($Peptide_{273-282}$) in Cl^- depicting helix fraying and mild cooperativity, respectively. Circles: experimental deuteration levels, normalized with in- and back-exchange levels. Grey dashed curves: hypothetical intrinsic uptake curves (PF = 1). On the top shows individual exponentials whose sum is fitted to the experimental values and plotted on the main buildup curves. Residues in grey denoted in the peptide sequence do not contribute to the deuterium uptake curve. **Upper right:** χ^2 and the relative error as the number of fit exponentials increases, used to assess the quality of fit. **Lower right:** Models and free energy surface of unfolding illustrating the difference between **(i)** fraying and **(ii)** mild cooperativity. **(B)** Mechanism for prestin's conformational transition from the expanded to the contracted state regulated by the anion concentration. Green rectangles and curved lines: folded and unfolded fractions, respectively, of TM3 and TM10. Blue filled circle: R399. Blue dashed circle: partial positive charges from TM3 and TM10 helical dipoles. Red filled circle: anions, with the size of the circle depicting anion concentrations. Black arrows: prestin's conformational change.

In contrast, we observed much more cooperative unfolding in prestin's lipid-facing helices, with exchange occurring from one or a few high energy states where a set of hydrogen bonds are broken concertedly. Cooperatively exchanging residues have similar PFs and a characteristic sigmoidal deuterium uptake curve for the associated peptide, as seen in prestin's intracellular portion of TM6 ($Region_{275-282}$: $Peptide_{273-282}$ + 4 peptides) (**Fig. 5A & Fig. S9.53-9.57**).

To characterize the degree of cooperativity for the HDX at the N-terminus of TM3 ($Peptide_{134-140}$) and the intracellular portion of TM6 ($Peptide_{273-282}$), we fit the deuterium uptake curves as a sum of exponentials[17], $D(t) = \sum_{i=1}^{n}(1 - e^{-k_i t})$, where k_i is the exchange rate and n is the number of exponentials, ranging from one to the number of exchange-competent residues. The value of n was determined by the quality of the fit, evaluated by χ^2 and having a relative error smaller than one (i.e., standard deviation for k_i less than k_i itself). HDX data for the N-terminus of prestin's TM3 ($Peptide_{134-140}$) was fit with four well-separated exponentials with rates spanning five log units for the four residues (**Fig. 5A**). The need to individually fit each site indicates a lack of cooperativity and helix fraying. In contrast, the peptide representing the intracellular portion of TM6 ($Peptide_{273-282}$) has eight residues yet it could be fitted with only three rates spanning less than two log units (**Fig. 5A**). This rather concerted deuterium uptake was independent of the anion substrate identity and also observed for TM1, TM5b, the intracellular portion of TM7, and the N-terminus of TM8 (**Fig. S9.6-9.16, S9.42-9.43, S9.45-9.51, S9.58-9.63, S9.78-9.79**).

We define a parameter $\sigma_{\Delta G}$ to quantify the degree of folding cooperativity. The value of $\sigma_{\Delta G}$ is calculated as the standard deviation for the free energies of unfolding (ΔGs) for exchange-competent residues comprising the peptide. When a region folds 100% cooperatively, $\sigma_{\Delta G}$ is zero as all residues have the same ΔG. As the diversity increases (lower cooperativity), the $\sigma_{\Delta G}$ value becomes larger. The accuracy of the ΔG determination at residue level can be increased by comparing uptake curves for overlapping peptides and/or deconvoluting isotope envelopes[17]. Here we assigned exchange rates (k_i), obtained from the fitting method mentioned above, to residues based on the directionality of helix fraying, with residues closer to the end of a helix

having faster rates. When there is ambiguity on which rate to assign to a given residue, the geometric mean of the rates was used (**Materials and Methods**). We found that prestin's intracellular portion of TM6 ($Peptide_{273-282}$) has $\sigma_{\Delta G}$ = 1.1, indicating mild cooperativity, whereas the non-cooperative N-terminal TM3 ($Peptide_{134-140}$) has a $\sigma_{\Delta G}$ = 2.9. This significant decrease in folding cooperativity for helices directly involved in the Cl^- binding site likely has functional consequences related to prestin's electromotility, as discussed below.

Discussion

Using HDX-MS, we provide novel information on the structural dynamics of prestin in its apo state, for which there isn't an associated cryo-EM structure. We have explored the energetic and conformational differences between prestin, a voltage-dependent motor, and its mammlian relative SLC26A9, a representative member of the SLC26 family of anion transporters for which a cryo-EM structure is available. Our data point to major differences in the energetics at the anion-binding site of prestin and SLC26A9 despite their structural similarities. This comparison addresses underlying mechanistic questions related to the unique properties of prestin, the origin of its voltage dependence, and the potential mechanisms that couple charge movements to electromotility.

We showed that prestin displays an unstable binding site that, upon Cl^- unbinding, unfolds by one helical turn at the electrostatic gap formed by the abutting (antiparallel) short helices TM3 and TM10 (**Fig. 2A & Fig. 3**). We measured an increase in local ΔΔG = 1.8~3.5 kcal/mol upon anion binding. This energy difference is within the range of the ΔΔG = 2.4 kcal/mol estimated from having a 60-fold excess of Cl^- above the EC_{50} (6 mM)[11]. Similar folding events upon anion binding are absent in SLC26A9 (**Fig. 2B**), pointing to a key role of the bound anion as a structural element in prestin, stabilizing the natural repulsion between TM3-TM10 positive helical macrodipoles. This phenomenon rationalizes the conundrum that prestin's voltage dependence requires the proximity of a bound anion to R399.

We find that anion binding to prestin mainly stabilizes the interface between the scaffold and the elevator domains (**Fig. 1C & Fig. S1A**). This phenomenon is consistent with an elevator-like mechanism during prestin's conformational transition from the expanded to the contracted state[5]. Anion binding stabilizes prestin's intracellular cavity and slightly destabilizes regions facing the extracellular matrix. This effect can result from changes in solvent exposure, as the intracellular water cavity may shrink as prestin contracts. For SLC26A9, the destabilization upon anion binding at the intracellular cavity likely results from a shift from the outward-facing state to the inward-facing state (**Fig. 1C & Fig. S1B**), supporting the alternate-access mechanism for this fast transporter[9,10]. Similar HDX changes, i.e., increased HDX on the intracellular side while slowed HDX on the extracellular side, have been observed in other transporters during their transition from outward-facing to inward-facing states[25,26]. Prestin's distinct HDX response compared to canonical transporters is consistent with it being an incomplete anion transporter[11,27].

The HDX data for prestin in Cl^-, SO_4^{2-}, and salicylate support an allosteric role for the anion binding at the TM3-TM10 electrostatic gap[12–14] (**Fig. 4**). SO_4^{2-} binding leads to shifts in the NLC

246 towards positive potentials, thus stabilizing multiple conformations that are on average more
247 expanded than prestin in Cl^- [5,13,28]. Since the binding of SO_4^{2-} to prestin is weaker than that of Cl^-
248 [6], the slight increase in HDX at the binding site likely reflects more prestin molecules adopting the
249 apo state. Salicylate binding inhibits prestin's NLC and yet the molecular basis of such inhibition
250 remains obscure[5,16]. Bavi *et al*[5] showed that binding of salicylate occludes prestin's binding
251 pocket from solvent and inhibits the movement of TM3 and TM10. This is fully consistent with
252 the 10-fold HDX slowing found for the N-termini of TM3 and TM10 upon salicylate binding as
253 compared to the rest of the protein. Our HDX data, together with results from Bavi *et al.*[5], suggest
254 that salicylate likely inhibits prestin's NLC by restricting the dynamics of the anion-binding site.

255 We identified helix fraying at the anion-binding site of prestin based on its broad
256 deuterium uptake curve in the presence of Cl^-, consistent with a multi-state landscape (**Fig. 5A**).
257 This fraying suggests that an increase in the anion concentration would promote helical
258 propensity at TM3 and TM10, and is inconsistent with a cooperative (two-state) model involving
259 an equilibrium between an apo state and a single bound state (**Fig. 5A**). Therefore, we suggest
260 that a two-state model of prestin's conformational changes with a high energy barrier would be
261 insufficient to explain its fast kinetics, whereas charge movement is facilitated by crossing
262 multiple shallow barriers[13,29].

263 We propose that having a Cl^- binding site that frays can promote prestin's fast motor
264 response which is thought to have evolved independently of its voltage sensing ability[30,31]. While
265 prestin's TM3 and TM10 have similar stability, SLC26A9 exhibits a non-fraying TM3 that is more
266 stable than TM10 (**Fig. 2**). Furthermore, the normally highly conserved Pro136 in mammalian
267 prestin is replaced with a Threonine in other vertebrates that express non-electromotile prestin
268 (**Fig. S4A**). This Pro136Thr substitution, based on our Upside MD simulations, results in a hyper-
269 stabilized TM3 that would otherwise have similar folding stability as TM10 (**Fig. S4B**). A Pro136Thr
270 mutation in rat prestin also leads to a shift of NLC towards depolarized potentials[18]. These
271 thermodynamic and functional consequences of having a destabilized TM3 with Pro136, which
272 now has similar stability as TM10, lead us to hypothesize that prestin's fast somatic motility may
273 be promoted by having simultaneous fraying of the TM3 and TM10 helices.

274 Helices that exhibit cooperative unfolding all appear to be lipid-facing helices, including
275 TM6-TM7, TM1, TM5b, and TM8. The region with the most pronounced cooperativity, the
276 intracellular portion of TM6, has a series of glycines including the consecutive G274-G275 pair
277 that underlies the "electromotility elbow", a helical bending contributing to the largest cross-
278 sectional area (expanded conformation) and the thin notch in the micelle[5]. The structural
279 consequences of cooperativity speak to the significance of these helices in prestin's area
280 expansion. We propose that cooperativity allows for long-range allostery[32] so that the lipid-facing
281 helices can adopt large-scale structural rearrangements as induced by voltage sensor movements,
282 thereby achieving rapid electromechanical conversions of prestin. The exact mechanism through
283 which cooperativity contributes to prestin's electromotility remains a key question.

284 Based on the structural and allosteric role of Cl^- binding at the TM3-TM10 electrostatic
285 gap, we propose a model in which prestin's conformational changes and electromotility are
286 regulated by the folding equilibrium of the anion-binding site (**Fig. 5B**). In our model, anion
287 binding participates in a local electrostatic balance that includes the positively charged R399 and

288 the positive TM3-TM10 helical macrodipoles. In the apo state, the anion-binding site unfolds due
289 to the electrostatic repulsion between these positively charged groups. Being a buried charge,
290 R399 may exit from the electric field concentrated in the lower dielectric environment of the
291 protein, and move into the solvent region as it lacks a neutralizing anion. This event is coupled to
292 the allosteric expansion of prestin's membrane footprint[5]. Anion binding partially neutralizes the
293 positive electric field at the binding site, an event that is coupled to the residue-by-residue folding
294 for the N-termini of TM3 and TM10 as well as the shortening of the electrostatic gap. This folding
295 event results in a more focused electric field and consequent contraction of prestin's
296 intermembrane cross-sectional area. At physiologically-relevant low Cl^- concentration (1.5-4
297 mM)[33], prestin's binding site is likely to be only partially folded. Complete folding may be
298 achieved by membrane potential acting on the TM3-TM10 helical dipoles, which leads to the
299 movement of the voltage sensor across the electric field and the rapid areal expansion for the
300 TMDs (i.e., electromotility).

301

302 **Conclusions**

303 We applied HDX-MS to the study of prestin's electromotility and identified folding events that
304 are likely critical for function but had escaped detection by cryo-EM. The folding equilibrium of
305 the Cl^- binding site and its dependence on Cl^- concentration appears to rationalize the conundrum
306 of how an anion that binds in proximity to a positive charge (R399), can enable the NLC of prestin.
307 We observed fraying of the helices forming the anion-binding site, which contrasts with
308 cooperative unfolding of the lipid-facing helices. We believe that the non-cooperative fraying of
309 the helices involved in voltage sensing may allow for fast charge movements within the electric
310 field. This heightened sensitivity of the voltage sensor then induces large-scale motions of the
311 lipid-facing helices, enabled by their cooperativity (or allostery), thereby altering the cross-
312 sectional area of prestin. These principles warrant further investigation.

313

314 **Meterials and Methods**

315 <u>Sample preparation for prestin and SLC26A9.</u> Generation of the dolphin prestin and mouse
316 SLC26A9 constructs, protein overexpression, and purification were conducted using the same
317 protocol as previously described[5]. Following the cleavage of the GFP tag, the protein was purified
318 by size-exclusion chromatography on a Superose 6, 10/300 GE column (GE Healthcare), with the
319 running buffer being either the "Cl^-/H_2O Buffer" or the "SO_4^{2-}/H_2O Buffer", including 1 µg/ml
320 aprotinin and 1 µg/ml pepstatin[5]. The "Cl^-/H_2O Buffer" contained 360 mM NaCl, 20 mM Tris, 3
321 mM dithiothreitol, 1 mM EDTA, and 0.02% GDN at pH 7.5. The "SO_4^{2-}/H_2O Buffer" contained 140
322 mM Na_2SO_4, 5 mM $MgSO_4$, 20 mM Tris, 0.02% GDN, and 10-15 mM methanesulfonic acid to
323 adjust the pH to 7.5. Peak fractions containing the sample were concentrated on a 100K MWCO
324 centrifugal filter (Millipore) to 2-3 mg/mL, flash-frozen in liquid nitrogen, and kept at −80 °C until
325 use.

326

327 Hydrogen-deuterium exchange. **Table S1** provides biochemical and statistical details for HDX in
328 this study. HDX reactions, quench, and injection were all performed manually. Prior to HDX,
329 proteins purified in Cl^- and SO_4^{2-} were buffer exchanged to the same H_2O buffer without protease
330 inhibitor using 7K MWCO Zeba spin desalting columns (Thermo 89882). For HDX conducted in
331 Hepes, proteins purified in Cl^- were dialyzed against the "Hepes/H_2O Buffer" (150 mM Hepes,
332 0.02% GDN, pH adjusted to 7.5 by Hepes acid or base) using a 10K MWCO dialysis device (Thermo
333 Slide-A-Lyzer MINI 69570) with three times of buffer exchange for near-complete Cl^- removal.
334 HDX in a solution of 93% deuterium (D) content was initiated by diluting 2 µL of 25 µM prestin or
335 SLC26A9 stock in an H_2O buffer into 28 µL of the corresponding buffer made with D_2O (99.9% D,
336 Sigma-Aldrich 151882). HDX was conducted in one of the two conditions: 1) pD_{read} 7.1, 25 °C; 2)
337 pD_{read} 6.1, 0 °C. The D_2O buffers contained the same compositions as the corresponding H_2O
338 buffers, except that Tris was replaced with Phosphate for the "SO_4^{2-}/D_2O Buffer" for both HDX
339 conditions, and the "Cl^-/D_2O Buffer" for HDX performed at pD_{read} 6.1, 0 °C. The pD_{read} was
340 adjusted to 7.1 or 6.1 by DCl for the "Cl^-/D_2O Buffers" and by NaOD for other D_2O buffers. For
341 HDX in the presence of salicylate, 50 mM salicylate acid was added to the "SO_4^{2-}/D_2O Buffer" and
342 the pD_{read} was adjusted by NaOD. For HDX in the presence of urea, 4 M urea was added to the
343 "Cl^-/D_2O Buffer" or the "Hepes/D_2O Buffer", with accurate urea concentration determined to be
344 4.16 M and 4.54 M, respectively, by refractive index using a refractometer (WAY Abbe)[34]. HDX
345 was quenched at various times, ranging from 1 s to 27 h, by the addition of 30 µL of ice-chilled
346 quench buffer containing 600 mM Glycine, 8 M urea, pH 2.5. For HDX in the presence of urea,
347 urea concentration in the quench buffer was adjusted to reach a 4 M final concentration.
348 Quenched reactions were immediately injected into a valve system maintained at 5 °C (Trajan
349 LEAP). Non-deuterated controls and MS/MS runs for peptide assignment were performed with
350 the same protocol as above except D_2O buffers were replaced by H_2O buffers, followed by the
351 immediate addition of the quench buffer and injection. HDX reactions were performed in random
352 order. No peptide carryover was observed as accessed by following sample runs with injections
353 of quench buffer containing 4 M urea and 0.01% GDN. In-exchange controls accounting for
354 forward deuteration towards 41.5% D in the quenched reaction were performed by mixing D_2O
355 buffer and ice-chilled quench buffer prior to the addition of the protein. Maximally labeled
356 controls ("All D") accounting for back-exchange were performed by a 48-h incubation with the
357 "Cl^-/D_2O Buffer" at 37 °C, followed by a 30-min incubation with 8 M of deuterated urea at 25 °C.

358

359 Protease digestion and LC-MS. Upon injection, the protein was digested online by a pepsin/FPXIII
360 (Sigma-Aldrich P6887/P2143) mixed protease column maintained at 20 °C. Protease columns
361 were prepared in-house by coupling the protease to a resin (Thermo Scientific POROS 20 Al
362 aldehyde activated resin 1602906) and hand-packing into a column (2 mm ID × 2 cm, IDEX C-
363 130B). After digestion, peptides were desalted by flowing across a hand-packed trap column
364 (Thermo Scientific POROS R2 reversed-phase resin 1112906, 1 mm ID × 2 cm, IDEX C-128) at 5 °C.
365 The total time for digestion and desalting was 2.5 min at 100 µL/min of 0.1% formic acid at pH
366 2.5. Peptides were then separated on a C18 analytical column (TARGA, Higgins Analytical, TS-
367 05M5-C183, 50 x 0.5 mm, 3 µm particle size) via a 14-min, 10–60% (vol/vol) acetonitrile (0.1%
368 formic acid) gradient applied by a Dionex UltiMate-3000 pump. Eluted peptides were analyzed
369 by a Thermo Q Exactive mass spectrometer. MS data collection, peptide assignments by

370 SearchGUI version 4.0.25, and HDX data processing by HDExaminer 3.1 (Sierra Analytics) were
371 performed as previously described[23,24].

372

373 HDX data presentation, quantification, and statistics. In our labeling convention, we name
374 capitalized regions according to the third residue of each peptide since the first two residues have
375 much faster k_{chem}[35,36] and hence, exhibit complete back-exchange. Labeling times for HDX
376 performed in pD_{read} 6.1, 0 °C were corrected to those in pD_{read} 7.1, 25 °C by a factor of 140,
377 determined by the ratio of the k_{chem} for full-length proteins in the two conditions – prestin:
378 $\tau_{chem}^{\mathrm{pDread\ 6.1,0\ °C}}$ = 10 sec, $\tau_{chem}^{\mathrm{pDread\ 7.1,25\ °C}}$ = 74 msec; SLC26A9: $\tau_{chem}^{\mathrm{pDread\ 6.1,0\ °C}}$ = 9 sec,
379 $\tau_{chem}^{\mathrm{pDread\ 7.1,25\ °C}}$ = 65 msec. Deuteration levels were adjusted with the 93% D content but not with
380 back-exchange levels except for **Fig. 5A**. For HDX in the presence of urea (**Fig. 3A**), D contents of
381 76% and 74% were used to account for the volumes of 4.16 M and 4.54 M urea in the "Cl^-/D_2O
382 Buffer" and the "Hepes/D_2O Buffer", respectively.

383 HDX rates, protection factors (PFs), and changes of free energy of unfolding (ΔΔG's) in the
384 Results section were estimated by fitting uptake curves of each peptide, after correcting for back-
385 exchange levels, with a stretched exponential as described by Hamuro 2021[17], except for
386 discussion relevant to **Fig. 5A**. Peptides with less than 10% D at the longest labeling time (~10^5 s)
387 were not used for fitting. The residue-level ΔΔG values presented in the full-length proteins in
388 **Fig. 1C** were estimated by averaging ΔΔG values for peptides containing the residue. We note
389 that this stretched exponential method is only a rough approximation to extract ΔΔG's and our
390 major conclusions are not dependent on this fitting method.

391 For fitting HDX data and extracting rates relevant to **Fig. 5A**, HDX data were first
392 normalized to in- and back-exchange levels. Given the helices are likely to exchange by fraying,
393 the exchange rate for each residue was assigned based on their distance from the end of the
394 helix. When a residue could not be assigned to a single rate, the geometric mean of the possible
395 rates was used, e.g., the HDX data for the 8-residue $Peptide_{273\text{-}282}$ were well fit with 3
396 exponentials, and the three associated rates, k_1, k_2, & k_3, were assigned to the 8 residues
397 according to k_1, k_1, $(k_1k_1k_2)^{1/3}$, k_2, k_2, $(k_2k_2k_3)^{1/3}$, k_3, & k_3. These rates were used to calculate folding
398 stability according to $\Delta G = -RT\ln(k_{chem}/k_i - 1)$.

399 A hybrid statistical analysis used to generate **Fig. S1** was performed as described by
400 Hageman & Weis, 2019[37], with significance limits defined at α = 0.05.

401

402 MD simulations. Simulations were conducted in our Upside molecular dynamics package[38,39]
403 using a membrane thickness of 38 Å. Missing residues for prestin (PDB 7S8X) were built using
404 MODELLER[40] and the placement within the bilayers was accomplished using Positioning of
405 Proteins in Membranes webserver[41]. Local restraints in the form of small springs between nearby
406 residues were used to maintain the native structure of cytosolic domains, as well as to the TM13-
407 TM14 helices. Also, the distance between the two TMDs was held fixed. We ran 28 temperature
408 replicas between 318 and 360K.

409

410 **Acknowledgments**

411 This work was supported by grants to T.R.S. from the NSF (MCB 2023077) and the NIH (GM55694,
412 1R35GM148233), and to E.P. from R01 DC019833.

References

1. Dallos, P., Zheng, J. & Cheatham, M. A. Prestin and the cochlear amplifier. *J. Physiol.* **576**, 37–42 (2006).
2. Sfondouris, J., Rajagopalan, L., Pereira, F. A. & Brownell, W. E. Membrane Composition Modulates Prestin-associated Charge Movement. *J. Biol. Chem.* **283**, 22473–22481 (2008).
3. Liberman, M. C. *et al.* Prestin is required for electromotility of the outer hair cell and for the cochlear amplifier. *Nature* **419**, 5 (2002).
4. Dong, X., Ospeck, M. & Iwasa, K. H. Piezoelectric Reciprocal Relationship of the Membrane Motor in the Cochlear Outer Hair Cell. *Biophys. J.* **82**, 1254–1259 (2002).
5. Bavi, N. *et al.* The conformational cycle of prestin underlies outer-hair cell electromotility. *Nature* **600**, 553–558 (2021).
6. Ge, J. *et al.* Molecular mechanism of prestin electromotive signal amplification. *Cell* **184**, 4669-4679.e13 (2021).
7. Butan, C. *et al.* Single particle cryo-EM structure of the outer hair cell motor protein prestin. *Nat. Commun.* 40 (2022).
8. Garaeva, A. A. & Slotboom, D. J. Elevator-type mechanisms of membrane transport. *Biochem. Soc. Trans.* **48**, 1227–1241 (2020).
9. Walter, J. D., Sawicka, M. & Dutzler, R. Cryo-EM structures and functional characterization of murine Slc26a9 reveal mechanism of uncoupled chloride transport. *eLife* **8**, e46986 (2019).
10. Chi, X. *et al.* Structural insights into the gating mechanism of human SLC26A9 mediated by its C-terminal sequence. *Cell Discov.* **6**, 55 (2020).
11. Oliver, D. *et al.* Intracellular Anions as the Voltage Sensor of Prestin, the Outer Hair Cell Motor Protein. *Science* **292**, 2340–2343 (2001).
12. Rybalchenko, V. & Santos-Sacchi, J. Cl− flux through a non-selective, stretch-sensitive conductance influences the outer hair cell motor of the guinea-pig. *J. Physiol.* **547**, 873–891 (2003).
13. Rybalchenko, V. & Santos-Sacchi, J. Anion Control of Voltage Sensing by the Motor Protein Prestin in Outer Hair Cells. *Biophys. J.* **95**, 4439–4447 (2008).
14. Song, L. & Santos-Sacchi, J. Conformational State-Dependent Anion Binding in Prestin: Evidence for Allosteric Modulation. *Biophys. J.* **98**, 371–376 (2010).
15. Bai, J.-P. *et al.* Prestin's Anion Transport and Voltage-Sensing Capabilities Are Independent. *Biophys. J.* **96**, 3179–3186 (2009).
16. Gorbunov, D. *et al.* Molecular architecture and the structural basis for anion interaction in prestin and SLC26 transporters. *Nat. Commun.* **5**, 3622 (2014).
17. Hamuro, Y. Quantitative Hydrogen/Deuterium Exchange Mass Spectrometry. *J. Am. Soc. Mass Spectrom.* **32**, 2711–2727 (2021).

18. Schaechinger, T. J. *et al.* A synthetic prestin reveals protein domains and molecular operation of outer hair cell piezoelectricity. *EMBO J.* **30**, 2793–2804 (2011).
19. Smit, J. H. *et al.* Probing Universal Protein Dynamics Using Hydrogen–Deuterium Exchange Mass Spectrometry-Derived Residue-Level Gibbs Free Energy. *Anal. Chem.* **93**, 12840–12847 (2021).
20. Santos-Sacchi, J. & Navaratnam, D. Physiology and biophysics of outer hair cells: The cells of Dallos. *Hear. Res.* 108525 (2022) doi:10.1016/j.heares.2022.108525.
21. Lim, W. K., Rösgen, J. & Englander, S. W. Urea, but not guanidinium, destabilizes proteins by forming hydrogen bonds to the peptide group. *Proc. Natl. Acad. Sci.* **106**, 2595–2600 (2009).
22. Ramesh, R. *et al.* Uncovering metastability and disassembly hotspots in whole viral particles. *Prog. Biophys. Mol. Biol.* **143**, 5–12 (2019).
23. Zmyslowski, A. M., Baxa, M. C., Gagnon, I. A. & Sosnick, T. R. HDX-MS performed on BtuB in E. coli outer membranes delineates the luminal domain's allostery and unfolding upon B12 and TonB binding. *Proc. Natl. Acad. Sci.* **119**, e2119436119 (2022).
24. Lin, X., Zmyslowski, A. M., Gagnon, I. A., Nakamoto, R. K. & Sosnick, T. R. Development of in vivo HDX-MS with applications to a TonB-dependent transporter and other proteins. *Protein Sci.* **31**, e4402 (2022).
25. Merkle, P. S. *et al.* Substrate-modulated unwinding of transmembrane helices in the NSS transporter LeuT. *Sci. Adv.* **4**, eaar6179 (2018).
26. Martens, C. *et al.* Direct protein-lipid interactions shape the conformational landscape of secondary transporters. *Nat. Commun.* **9**, 4151 (2018).
27. Schaechinger, T. J. & Oliver, D. Nonmammalian orthologs of prestin (SLC26A5) are electrogenic divalent/chloride anion exchangers. *Proc. Natl. Acad. Sci.* **104**, 7693–7698 (2007).
28. Muallem, D. & Ashmore, J. An Anion Antiporter Model of Prestin, the Outer Hair Cell Motor Protein. *Biophys. J.* **90**, 4035–4045 (2006).
29. Santos-Sacchi, J., Navarrete, E. & Song, L. Fast Electromechanical Amplification in the Lateral Membrane of the Outer Hair Cell. *Biophys. J.* **96**, 739–747 (2009).
30. Tan, X. *et al.* A motif of eleven amino acids is a structural adaptation that facilitates motor capability of eutherian prestin. *J. Cell Sci.* **125**, 1039–1047 (2012).
31. Tang, J., Pecka, J. L., Fritzsch, B., Beisel, K. W. & He, D. Z. Z. Lizard and Frog Prestin: Evolutionary Insight into Functional Changes. *PLoS ONE* **8**, e54388 (2013).
32. Hilser, V. J. & Thompson, E. B. Intrinsic disorder as a mechanism to optimize allosteric coupling in proteins. *Proc. Natl. Acad. Sci.* **104**, 8311–8315 (2007).
33. McPherson, D. R. Sensory Hair Cells: An Introduction to Structure and Physiology. *Integr. Comp. Biol.* **58**, 282–300 (2018).
34. Warren, J. R. & Gordon, J. A. On the Refractive Indices of Aqueous Solutions of Urea. *J. Phys. Chem.* **70**, 297–300 (1966).
35. Bai, Y., Milne, J. S., Mayne, L. & Englander, S. W. Primary Structure Effects on Peptide Group Hydrogen Exchange. *Proteins* **17**, 75–86 (1993).
36. Nguyen, D., Mayne, L., Phillips, M. C. & Englander, S. W. Reference parameters for protein hydrogen exchange rates. *J. Am. Soc. Mass Spectrom.* **29**, 1936–1939 (2018).

37. Hageman, T. S. & Weis, D. D. Reliable Identification of Significant Differences in Differential Hydrogen Exchange-Mass Spectrometry Measurements Using a Hybrid Significance Testing Approach. *Anal. Chem.* **91**, 8008–8016 (2019).
38. Jumper, J. M., Faruk, N. F., Freed, K. F. & Sosnick, T. R. Accurate calculation of side chain packing and free energy with applications to protein molecular dynamics. *PLOS Comput. Biol.* **14**, e1006342 (2018).
39. Jumper, J. M., Faruk, N. F., Freed, K. F. & Sosnick, T. R. Trajectory-based training enables protein simulations with accurate folding and Boltzmann ensembles in cpu-hours. *PLOS Comput. Biol.* **14**, e1006578 (2018).
40. Sali, A. & Blundell, T. L. Comparative protein modelling by satisfaction of spatial restraints. *J. Mol. Biol.* **234**, 779–815 (1993).
41. Lomize, A. L., Todd, S. C. & Pogozheva, I. D. Spatial arrangement of proteins in planar and curved membranes by PPM 3.0. *Protein Sci. Publ. Protein Soc.* **31**, 209–220 (2022).